ACS Catalysis

Letter

pubs.acs.org/acscatalysis

Controlled Surface-Assembly of Nanoscale Leaf-Type Cu-Oxide Electrocatalyst for High Activity Water Oxidation

Khurram S. Joya*[,†,‡] and Huub J. M. de Groot[†]

[†]Leiden Institute of Chemistry, Leiden University, Einsteinweg 55, P.O. Box 9502, 2300 RA Leiden, The Netherlands

[‡]Department of Chemistry, University of Engineering and Technology (UET), GT Road, 54890 Lahore, Punjab, Pakistan

Supporting Information

ABSTRACT: The controlled surface deposition of a robust and high-performance nanostructured copper-oxide ($\mathbf{CuO_x}$-NLs) electrocatalyst for water oxidation is presented. The material exhibits a characteristic leaf-type morphology and self-assembles on a copper substrate by straightforward constant-current anodization. The oxygen onset occurs at about 1.55 V versus RHE (η = 320 mV), which is 400−500 mV less than for amorphous Cu-oxide films. A Tafel slope of 44 mV dec^{-1} is obtained, which is the lowest observed relative to other copper-based materials. Long-term catalytic performance and stability tests of the electrocatalytic $\mathbf{CuO_x}$-NLs sample show a stable current density of >17 mA cm^{-2} for oxygen evolution, which was sustained for many hours.

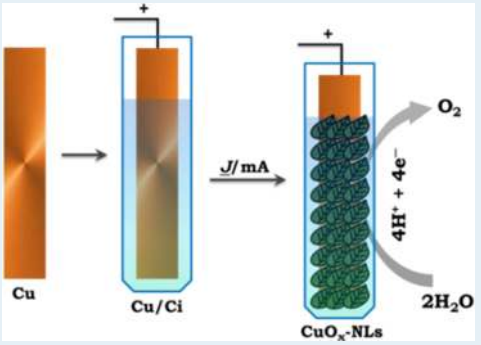

KEYWORDS: *electrocatalyst, water oxidation, copper-oxide, nanoscale leaves, oxygen evolution*

There are continuous efforts to develop a strategy to produce renewable and cleaner energy carriers from abundant solar radiation and water.[1,2] In this quest, catalytic water oxidation is regarded as a primary process, and many inorganic materials and transition metal-oxides are considered good candidates for this conversion.[2,3] Metal-oxide catalysts can be electrodeposited on conducting substrates from carbonate, phosphate, or borate electrolytes in the presence of metal ions.[4−6] To eliminate the possibility for interaction of metal ions with the cathodic sites during electrolysis, membranes or separators are usually employed that make the system more complex and introduce resistance and diffusion limitations in the electrochemical process.[7] New preparation methods are required that are easily implemented, and catalytic materials are desired to perform in metal ion free systems for sustained electrochemical operation.[8,9] In addition, control over the catalyst morphology and surface structure is important to induce a high surface area and phase purity, facilitating both charge transfer and mass transport during catalysis reaction.[9,10]

Stable and efficient metal-oxide derived electrocatalysts can develop in a carbonate/bicarbonate system under mild conditions.[5,11] HCO_3^-/CO_3^{2-} is suggested to facilitate proton management and prevent the degradation of these catalytic materials under anodic conditions.[12−14] We observed that anodization of a copper electrode via repetitive potential-sweeps or at constant-potential in a carbonate buffer induces the formation of very small copper-oxide particulate materials ($\mathbf{CuO_x}$-NPs) having oxygen onset at ∼1.59 V versus RHE ($\eta \geq$ 360 mV). In addition, we found that nanoscale leaf-shaped Cu-oxide ($\mathbf{CuO_x}$-NLs) surface structures (Figure S1) are formed during controlled anodization of a chemically etched copper substrate at a constant current density of 4.0 mA cm^{-2} in a carbonate system. The $\mathbf{CuO_x}$-NLs exhibit a remarkably low overpotential for water oxidation (η = 320 mV) relative to other Cu-based electrocatalysts[13−15] and many inorganic materials.[16,17]

Scanning electron microscopy (SEM) imaging shows a leaves-type copper-oxide matrix (Figure 1a). Individual leaflets are around 250 nm long and 60−70 nm wide (Figure 1b and S2). In contrast, copper oxide films produced by repetitive CV scans or via constant-potential surface anodization on native Cu-foil reveal a particulate-type structural morphology (Figure 1c) with particle sizes around 70 nm (Figure 1d). We ascribe the uniform surface-generation of $\mathbf{CuO_x}$-NLs on Cu-substrate to a controlled surface electrochemical process involving Cu oxidation to form Cu^{n+} type surface species that quickly turn into a metal hydroxide/oxide type composition on the etched metal substrate during the metal-oxide deposition phase (Figure S3).

XPS (X-ray photoelectron spectroscopy) data are characteristic for Cu(II)-oxides on a pure copper metal surface. The binding energy (BE) region between 928 and 965 eV shows the response from the Cu $2p_{3/2}$ and Cu $2p_{1/2}$ core levels at 933.8 and 953.8 eV, respectively (Figure S4).[18] A high BE of 933.8 eV for the Cu $2p_{3/2}$ confirms the presence of Cu^{2+} species.[19] The difference between the Cu $2p_{3/2}$ and Cu $2p_{1/2}$ levels is about 20 eV, which is in good agreement with data for the spin−orbit splitting reported for CuO preparations.[20] These observations

Received: December 25, 2015
Revised: February 10, 2016

DOI: 10.1021/acscatal.5b02950
ACS Catal. 2016, 6, 1768−1771

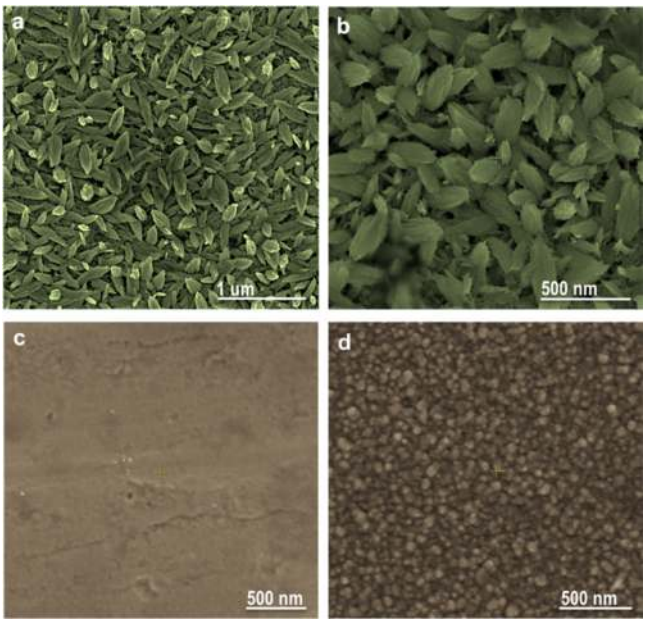

Figure 1. Scanning electron microscopy images for (a,b) the $\mathbf{CuO_x}$-NLs samples; (c) the simple Cu foil and for (d) nanoparticulate copper-oxide film.

are representative XPS signatures of the presence of Cu(II) derived metal-oxides.[21] Next to the Cu $2p_{3/2}$ XPS signal, there are two overlapping satellite peaks at higher BE between 940 and 943.9 eV (Figure S4b). These satellite peaks are characteristic of Cu^{2+} materials with a d9 configuration in the ground state (absent in case of Cu_2O) and are in good agreement with the values reported for Cu 2p levels in CuO phase.[22] The $\mathbf{CuO_x}$-NLs sample exhibits a lattice O 1s peak at binding energy of 531.8 eV that is attributed to a surface-bound hydroxide species originating from adsorbed H_2O molecules on the surface of the CuO-based film (Figure S4c).[20]

EDX (energy dispersive X-ray) measurements for the bulk elemental composition show Cu and O with a 1:1 ratio in the $\mathbf{CuO_x}$-NLs film (Figure S5). There is about 9% carbon content, which is thought to contribute to inducing high surface area, good electron transport, and enhanced structural flexibility.[23] The Raman spectrum for the $\mathbf{CuO_x}$-NLs reveals a $\mathbf{CuO_x}$ Ag band at approximately 295 cm^{-1} (Figure S6). The weak response at 340−344 cm^{-1} and a broad strong band centered at 628.5 cm^{-1} are assigned to the 2Bg modes in the metal-oxide. The Raman frequencies are well in line with data for pure single-phase $\mathbf{CuO_x}$ films having good crystallinity.[24]

Cyclic voltammetry shows the onset of the catalytic water oxidation current at 1.55 V (vs RHE) that grows rapidly and reaches >50 mA cm^{-2} under 1.84 V vs RHE (Figure 2). This O_2 onset potential is the lowest reported for electrogenerated Cu-oxide-derived water oxidation electrocatalysts.[13,14] Extended potential sweeping to 2.1 V vs RHE strongly increases the current density, which approaches 200 mA cm^{-2} on the $\mathbf{CuO_x}$-NLs-based electrode surface (Figure S7). A magnified CV view shows a copper oxidation polarization prefeature between 0.7−0.9 V, followed by a small potential window of steady current and the pronounced catalytic wave at ca. 1.55 V (inset Figure 2). The oxidative prefeature can be attributed to the surface oxidation of metallic copper Cu^0 into Cu^I, and leading to Cu^{II} type species with potential increment.[25,26]

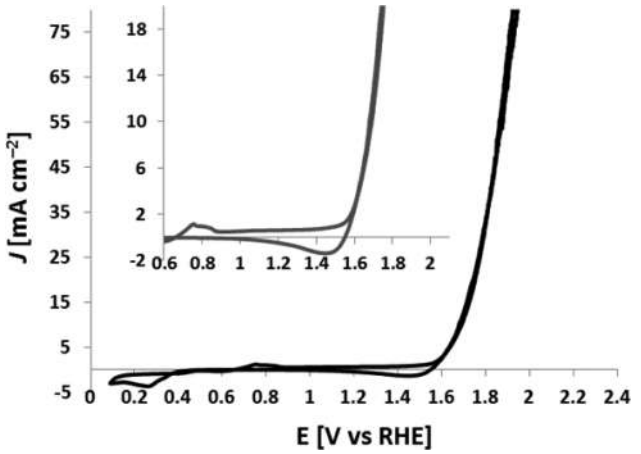

Figure 2. Cyclic voltammetry for the $\mathbf{CuO_x}$-NLs electrocatalyst in 0.2 M carbonate buffer (pH ∼ 11). Inset shows the magnified view of the CV (0.6−2.1 V).

The repetitive potential sweeps reproduce similar current density signatures on the 1st, 100th, and 500th CV scan, indicating little degradation or loss of performance of the $\mathbf{CuO_x}$-NLs system during electrocatalysis (Figure 3). For the

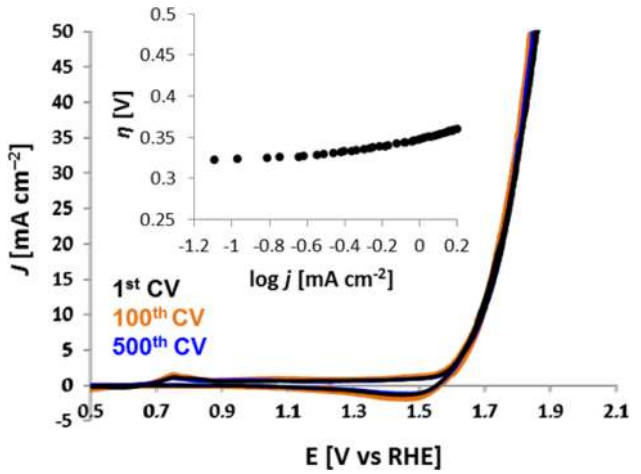

Figure 3. Concurrent 1st, 100th, and 500th CV sweeps for the $\mathbf{CuO_x}$-NLs. Inset shows Tafel plot during oxygen evolution.

Cu-oxide NPs type catalytic film, CV produces a higher O_2 onset potential of ∼1.59 V (vs RHE), observed during water oxidation (Figure S8). Also there is relatively low catalytic activity of the $\mathbf{CuO_x}$-NPs electrocatalyst compared to $\mathbf{CuO_x}$-NLs in the higher potential regime and a current density of 50 mA cm^{-2} is obtained at >2.0 V (vs RHE). The current−overpotential (η vs log (i) plot of the $\mathbf{CuO_x}$-NLs during OER produces a Tafel slope of 44 mV dec^{-1} (inset Figure 3). This Tafel slope is distinct for the $\mathbf{CuO_x}$-NLs based electrocatalyst as the $\mathbf{CuO_x}$-NPs presented here and other Cu-oxide based electrocatalytic systems show much higher Tafel slopes (Figure S9).[13,14,25] A small Tafel slope is representative of well-balanced kinetics over all steps of the entire conversion chain. The slow increase of the Tafel slope at higher voltages is attributed to increasing internal resistance. The system is characterized by high charge transfer rates, and a high density of active catalyst sites accumulated during anodic polarization. There is also good mass transfer from the open structural morphology and

DOI: 10.1021/acscatal.5b02950
ACS Catal. 2016, 6, 1768−1771

high crystallinity of the catalytic phase supporting electron transfer without scattering losses.[9,23] In addition, the broad enhanced Raman response for the collective Bg mode at 629.5 cm^{-1} suggests the possibility for vibrationally assisted catalysis for avoiding transfer losses and potential drop in the catalytic sites when increasing the rate.[27]

For the long-term performance and stability test of the electrocatalytic **CuO_x**-NLs, controlled-potential water electrolysis (CPE) and controlled-current electrolysis (CCE) are conducted in carbonate electrolyte. CPE at 1.81 V ($\eta \approx 580$ mV) shows an excellent and sustained oxygen evolution current density approaching 17 mA cm^{-2} (Figure 4a). The current density during 20 h remains highly stable with no noticeable decrease in catalytic performance. On the **CuO_x**-NPs system, the observed O_2 evolution current density is 5.2 mA cm^{-2} during the CPE run. The current density for **CuO_x**-NLs layers is more than 3 times higher than for the **CuO_x**-NPs film (Figure 4a). For the **CuO_x**-NLs sample, online oxygen measurements show 955 μmol of O_2 generation in 10 h of CPE with a Faradaic efficiency of >98%, corresponding to an oxygen generation rate of ~95.5 μmol per hour, and about 39 μmol of oxygen per hour for the as-prepared **CuO_x**-NPs (Figure S10).

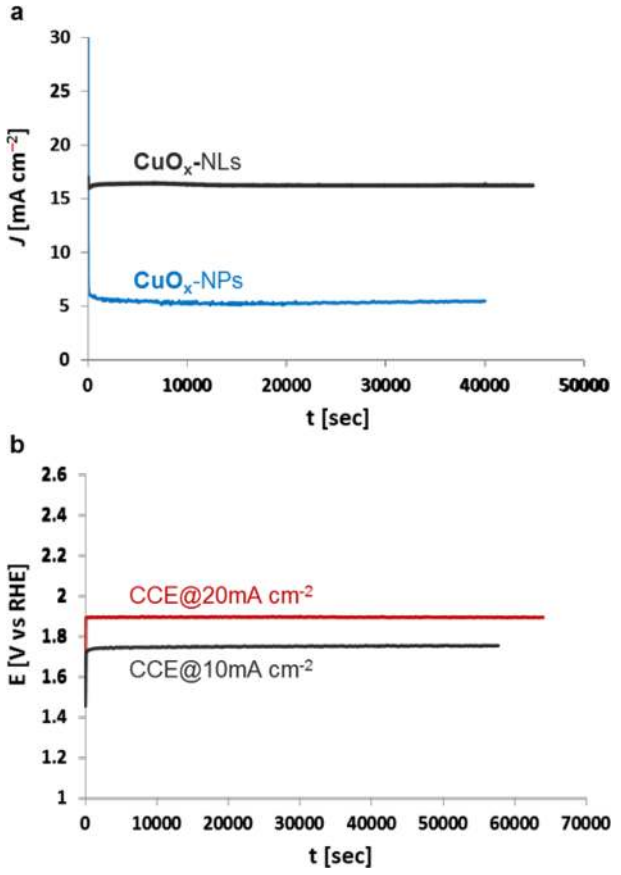

Figure 4. Extended period water oxidation during (a) controlled potential electrolysis using **CuO_x**-NLs and as-prepared **CuO_x**-NPs at 1.81 V vs RHE; and (b) constant current water electrolysis for the **CuO_x**-NLs based electrocatalyst at J = 10 mA cm^{-2} and 20 mA cm^{-2}, in carbonate buffer.

During constant current electrolysis, the **CuO_x**-NLs sample remains remarkably stable for water oxidation at current densities of 10 mA cm^{-2} and 20 mA cm^{-2}. To achieve 10 mA cm^{-2}, a very stable steady-state potential of ~1.75 V (vs RHE) is preserved for more than 20 h of water electrolysis (Figure 4b). Similarly, a current density of 20 mA cm^{-2} is maintained at just ~1.88 V (vs RHE) in a clean carbonate system. There is no observable catalytic degradation and change in the voltage during CCE, which is a direct indication of the stability and sustained catalytic activity of the **CuO_x**-NLs.

In summary, we have deposited a copper-oxide based electroactive material via controlled current anodization in a clean carbonate system (pH ≈ 11) that forms a stable and high-performance water oxidation electrocatalyst. The **CuO_x**-NLs are crystalline, and no surface treatment, electrochemical conditioning, or pre/post- annealing procedures are required to develop them. Oxygen evolution initiates at a very low overpotential (η = 320 mV), and an oxygen evolution current density of 10 mA cm^{-2} is achieved at 1.68 V (vs RHE). The current density remains stable during long-term testing for catalytic performance, and catalysis operation can be sustained for more than 24 h. The high catalytic activity of the **CuO_x**-NLs electrocatalyst in carbonate solution is attributed to the leaf-type convex nanostructured surface morphology, presence of carbon contents in the film, and the pure phase crystallinity with a characteristic vibrational structure of the collective Bg oxygen modes. Coupling of oxygen vibration to electronic charge transfer may facilitate catalysis and electron spin alignment for O−O bond formation with the Cu in a d9 ground state. The high catalytic rate of the **CuO_x**-NLs system also confirms the synergistic role of the carbonate for electron transport in the catalytic cycle, while the strong catalytic response suggests a mediating role of the alkaline surrounding in the proton management.[12] The high current density that can be achieved in this way is a step forward in the quest for solar to chemical energy conversion via water splitting.[28,29]

■ ASSOCIATED CONTENT

Ⓢ Supporting Information

The Supporting Information is available free of charge on the ACS Publications website at DOI: 10.1021/acscatal.5b02950.

SEM, XPS, EDX, Raman spectra, and supporting electrochemical measurements and data (PDF)

■ AUTHOR INFORMATION

Corresponding Author

*E-mail: khurram_joya@uet.edu.pk.

Notes

The authors declare no competing financial interest.

■ ACKNOWLEDGMENTS

K.S.J. acknowledges research support from HEC-PAK and Leiden University/BioSolar Cells Program.

■ REFERENCES

(1) Smith, R. D. L.; Sporinova, B.; Fagan, R. D.; Trudel, S.; Berlinguette, C. P. *Chem. Mater.* **2014**, *26*, 1654−1659.

(2) Joya, K. S.; Morlanés, N.; Maloney, E.; Rodionov, V.; Takanabe, K. *Chem. Commun.* **2015**, *51*, 13481−13484.

(3) Dau, H.; Limberg, C.; Reier, T.; Risch, M.; Roggan, S.; Strasser, P. *ChemCatChem* **2010**, *2*, 724−761.

(4) Kanan, M. W.; Nocera, D. G. *Science* **2008**, *321*, 1072−1075.

(5) Joya, K. S.; Joya, Y. F.; de Groot, H. J. M. *Adv. Energy Mater.* **2014**, *4*, 1301929.

(6) Dincă, M.; Surendranath, Y.; Nocera, D. G. *Proc. Natl. Acad. Sci. U. S. A.* **2010**, *107*, 10337−10341.

DOI: 10.1021/acscatal.5b02950
ACS Catal. 2016, 6, 1768−1771

(7) Joya, K. S.; Vallés-Pardo, J. L.; Joya, Y. F.; Eisenmayer, T.; Thomas, B.; Buda, F.; de Groot, H. J. M. *ChemPlusChem* **2013**, *78*, 35−47.
(8) Schlögl, R. *Angew. Chem., Int. Ed.* **2015**, *54*, 3465−3520.
(9) Pickrahn, K. L.; Park, S. W.; Gorlin, Y.; Lee, H.-B.-R.; Jaramillo, T. F.; Bent, S. F. *Adv. Energy Mater.* **2012**, *2*, 1269−1277.
(10) Joya, K. S.; de Groot, H. J. M. *ChemSusChem* **2014**, *7*, 73−76.
(11) Joya, K. S.; Takanabe, K.; de Groot, H. J. M. *Adv. Energy Mater.* **2014**, *4*, 1400252.
(12) Koroidov, S.; Shevela, D.; Shutova, T.; Samuelsson, G.; Messinger, J. *Proc. Natl. Acad. Sci. U. S. A.* **2014**, *111*, 6299−6304.
(13) Yu, F.; Li, F.; Zhang, B.; Li, H.; Sun, L. *ACS Catal.* **2015**, *5*, 627−630.
(14) Du, J.; Chen, Z.; Ye, S.; Wiley, B. J.; Meyer, T. J. *Angew. Chem., Int. Ed.* **2015**, *54*, 2073−2078.
(15) Li, T.-T.; Cao, S.; Yang, C.; Chen, Y.; Lv, X.-J.; Fu, W.-F. *Inorg. Chem.* **2015**, *54*, 3061−3067.
(16) Young, E. R.; Nocera, D. G.; Bulovic, V. *Energy Environ. Sci.* **2010**, *3*, 1726−1728.
(17) Deng, X.; Tüysüz, H. *ACS Catal.* **2014**, *4*, 3701−3714.
(18) Wanger, C. D.; Riggs, W. M.; Davis, L. E.; Moulder, J. F.; Muilenberg, G. E. *Handbook of X-Ray Photoelectron Spectroscopy: a reference book of standard data for use in x-ray photoelectron spectroscopy*; PerkinElmer Corp., Physical Electronics Division: Eden Prairie, Minnesota, 1979; pp 80−82.
(19) Morales, J.; Sánchez, L.; Martín, F.; Ramos-Barrado, J. R.; Sánchez, M. *Electrochim. Acta* **2004**, *49*, 4589−4597.
(20) Devaraj, M.; Deivasigamani, R. K.; Jeyadevan, S. *Colloids Surf., B* **2013**, *102*, 554−561.
(21) Biesinger, M. C.; Lau, L. W. M.; Gerson, A. R.; Smart, R. S. C. *Appl. Surf. Sci.* **2010**, *257*, 887−898.
(22) Iijima, Y.; Niimura, N.; Hiraoka, K. *Surf. Interface Anal.* **1996**, *24*, 193−197.
(23) Mao, S.; Lu, G.; Chen, J. *Nanoscale* **2015**, *7*, 6924−6943.
(24) Lu, Y.; Qiu, K.; Zhang, D.; Lin, J.; Xu, J.; Liu, X.; Tang, C.; Kim, J.-K.; Luo, Y. *RSC Adv.* **2014**, *4*, 46814−46822.
(25) Chen, Z.; Meyer, T. J. *Angew. Chem., Int. Ed.* **2013**, *52*, 700−703.
(26) González, S.; Pérez, M.; Barrera, M.; González Elipe, A. R.; Souto, R. M. *J. Phys. Chem. B* **1998**, *102*, 5483−5489.
(27) Purchase, R. L.; de Groot, H. J. M. *Interface Focus* **2015**, *5*, 20150014.
(28) Joya, K. S.; Joya, Y. F.; Ocakoglu, K.; van de Krol, R. *Angew. Chem.* **2013**, *125*, 10618−10630; *Angew. Chem., Int. Ed.* **2013**, *52*, 10426−10437.
(29) De Respinis, M.; Joya, K. S.; de Groot, H. J. M.; D'souza, F.; Smith, W.; van de Krol, R.; Dam, B. *J. Phys. Chem. C* **2015**, *119*, 7275−7281.

DOI: 10.1021/acscatal.5b02950
ACS Catal. 2016, 6, 1768−1771